

HYPERSPECTRAL IMAGE FUSION

Charis Lanaras, Emmanuel Baltsavias, Konrad Schindler

ETH Zurich, Institute of Geodesy and Photogrammetry, Stefano-Franscini-Platz 5, 8093 Zurich, Switzerland
{lanaras, manos, schindler}@geod.baug.ethz.ch

KEY WORDS: hyperspectral, image fusion, super-resolution, spectral unmixing, relative spectral response

ABSTRACT: In this research, we jointly process high spectral and high geometric resolution images, exploiting their synergies, with aims to (a) generate a fused image of high spectral *and* geometric resolution, and (b) to improve spectral unmixing level of hyperspectral images at subpixel regarding the estimation of endmembers and fractional abundances. The potential of this methodological improvement lies in a more accurate and detailed semantic interpretation of objects and their properties in hyperspectral and multispectral images, with applications often in environmental mapping, monitoring and change detection. To incorporate the case of real data the spectral response of the one sensor with respect to the other must be known. To estimate the relative spectral response the two images must be co-registered and the point spread function must be taken into account. In this paper, we degrade the images spectrally and geometrically so that they have the same dimensions and we solve a least-squares problem with two constraints. The results using synthetic data confirm this approach, while with real data results are in principle promising, but in some cases the reconstructed spectral response is noisy.

1. INTRODUCTION

The aim of this work is the integrated processing of (a) high spectral resolution images (HSRI) with low geometric resolution, and (b) high geometric resolution images (HGRI) with low spectral resolution. From two such images, three products can be generated. Firstly, a fused image with both high spectral and geometric resolution is generated, which can be thought of as a sort of hyperspectral pan-sharpening, improved through the use of spectral unmixing constraints. Secondly, a better spectral unmixing of the HSRI, through integration of geometric information from the HGRI. Thirdly, due to the spectra overlap, the relative spectral response of the two sensors can be computed.

Hyperspectral imaging, often also called imaging spectroscopy, delivers HSRI with many (up to several hundreds) contiguous spectral bands of narrow (few nm) bandwidth, covering the range of 400 nm to 700-2500 nm, but have low geometric resolution. The HGRI are typically multispectral images with often only 3 to 4 bands in the RGB and NIR bands, with a wide bandwidth of several tens of nm. HSRI are increasingly available, especially from airborne, satellite and lately also terrestrial platforms. HGRI are widely acquired from all kind of platforms. These two types of images are partly complementary, but have rarely been processed jointly. Merging them into a single, enhanced image product is sometimes termed “hyperspectral image fusion” or “hyperspectral super-resolution”.

The main aim of the proposed method is a more accurate and detailed semantic information extraction. HSRI can distinguish finer spectral differences among objects, thus, more objects can be localized and classified, e.g. for land-cover mapping, and also biophysical/biochemical properties of objects can be better estimated. Since HSRI have a large GSD, mixed pixels occur more often, especially in urban areas. Unmixing determines for each pixel the “endmembers” (so called “pure” material spectra) and the “fractional abundances” (proportional contribution of each endmember within the pixel). The abundances and endmembers are subject to several physical constraints, like that the abundances for all endmembers in a pixel must be non-negative and sum to 1, while the number of endmembers present within each pixel, is rather low. The contribution of HGRI in the unmixing is due to the higher geometric resolution. Geometric information from the HGRI, e.g. homogeneous segments, edges and texture boundaries, can lead to a more accurate unmixing, and also a spatial localization of the abundances; instead of estimating simply the percentage of one endmember within a pixel, one can localize the corresponding areas (i.e. the pixels at the higher HGRI resolution).

In order to perform the hyperspectral image fusion one needs to know the relative spectral response of the two sensors. For this there are two options. The first option would be to compute this relative spectral response from the information the manufacturer gave about them. The second option would be to estimate it from the existing data. Since the hyperspectral sensor is recording detailed information about the spectrum one could integrate over the hyperspectral channels that form one multispectral channel. In this way, we reduce the prior knowledge needed about the sensors and perform the fusion without this information. This can be useful especially in the cases where the sensor is spaceborne and it is likely that the spectral response might have changed compared to the prelaunch values. We present a method that is resilient against radiometric noise and coregistration errors.

2. RELATED WORK

Most methods for *hyperspectral data fusion* rely on some form of matrix factorization. Yokoya et al. (2012) use VCA to extract endmembers with and then apply a Non-negative Matrix Factorization (NMF) to jointly estimate endmembers and abundances for both a HSRI and a HGRI in an iterative manner. Akhtar et al. (2014) form a spectral basis in advance, and with the basis fixed they learn a sparse code for the image using a non-negative OMP (Orthogonal Matching Pursuit). Wycoff et al. (2013) introduce a non-negative sparsity-promoting framework, which is solved with the ADMM (Alternating Direction Method of Multipliers) solver. Bayesian approaches (Hardie et al., 2004, Wei et al., 2014) perform Maximum A Posteriori (MAP) inference by imposing priors on the distribution of image intensities.

Simoes et al. (2015) not only formulated a convex regularization problem using a fixed subspace for the spectral vectors to solve fusion. Additionally, they also estimate the spectral response and spatial blur from the data, however not including any non-negativity constraints. On the other hand, for estimating the spectral response Yokoya et al. (2013) take into account non-negativity, but require prior knowledge about the spectral response. The problem is formulated in a way that returns a solution which only changes the initially known response up to some extent.

3. METHODOLOGY

3.1 Hyperspectral - Multispectral fusion

In earlier work (Lanaras et al., 2015) we have already developed a method for combined hyperspectral fusion and spectral unmixing. For completeness, we briefly summarize the basic model here. The goal of fusion is to combine information coming from a hyperspectral image (HSRI) $\bar{\mathbf{H}} \in \mathbb{R}^{w \times h \times B}$ and a multispectral image (HGRI) $\bar{\mathbf{M}} \in \mathbb{R}^{W \times H \times b}$. The HSRI has high spectral resolution, with B spectral bands, but low geometric resolution with w, h , image width and height respectively. The HGRI has high geometric resolution, with W, H , image width and height respectively, but a low spectral resolution b . We want to estimate a fused image $\bar{\mathbf{Z}} \in \mathbb{R}^{W \times H \times B}$ that has both high geometric and high spectral resolution. For this fused image we expect to have the spectral resolution of the HSRI (a lot larger than the HGRI, $B \gg b$) and the geometric resolution of the HGRI (a lot larger than the HSRI, $W \gg w$ and $H \gg h$).

To simplify the notation, we treat each image (“data cube”) as a matrix, with each row holding all pixels of an image in a certain spectral band, i.e. $N_h = wh$ and $N_m = WH$ pixels per row, while each matrix column shows all spectral values for a given pixel. Accordingly, the images are written $\mathbf{Z} \in \mathbb{R}^{B \times N_m}$, $\mathbf{H} \in \mathbb{R}^{B \times N_h}$ and $\mathbf{M} \in \mathbb{R}^{b \times N_m}$.

Following the LMM (Keshava and Mustard, 2002, Bioucas-Dias et al., 2012), mixing occurs additively within each pixel and the spectral response $\mathbf{z} \in \mathbb{R}^B$ of a given pixel of \mathbf{Z} is approximated as

$$\mathbf{z} = \sum_{j=1}^p \mathbf{e}_j a_j \quad (1)$$

where $\mathbf{e}_j \in \mathbb{R}^B$ denotes the spectral measurement (e.g. reflectance) of the $j \in \{1, \dots, p\}$ endmember, a_j denotes the *fractional abundance* of the respective endmember j , and p is the number of endmembers used to explain this pixel. Eq. (1) can be rewritten in matrix form:

$$\mathbf{Z} = \mathbf{E}\mathbf{A} \quad (2)$$

where $\mathbf{E} \equiv [\mathbf{e}_1, \mathbf{e}_2, \dots, \mathbf{e}_p]$, $\mathbf{E} \in \mathbb{R}^{B \times p}$, $\mathbf{A} \equiv [\mathbf{a}_1, \mathbf{a}_2, \dots, \mathbf{a}_{N_m}]$, $\mathbf{A} \in \mathbb{R}^{p \times N_m}$ and $\mathbf{a}_i \in \mathbb{R}^p$ are the fractional abundances for every pixel $i = \{1, 2, \dots, N_m\}$. By using this expression, we are able to represent the image \mathbf{Z} in a basis spanned by the endmembers, with the abundances as coefficients. Given that $p < B$, we are able to describe \mathbf{Z} in a lower dimensional space, thus achieving a dimensionality reduction. The assumption that $p < B$ and consequently that the data “live” in a lower dimensional space holds in most hyperspectral images and thus $\text{rank}\{\mathbf{Z}\} \leq p$.

3.1.1 Constraints. The basic idea of the proposed fusion and unmixing is to use the fact that in (1) the endmembers and abundances have a physical meaning and they can retain this meaning only under the following constraints:

$$\begin{aligned} a_{ij} &\geq 0 \quad \forall i, j && \text{(non-negative abundance)} \\ \mathbf{1}^\top \mathbf{A} &= \mathbf{1}^\top && \text{(abundances sum to 1)} \\ 0 &\leq e_{ij} \leq 1 \quad \forall i, j && \text{(non-negative, bounded reflectance)} \end{aligned} \quad (3)$$

with e_{ij} and a_{ij} the elements of \mathbf{E} , respectively \mathbf{A} . $\mathbf{1}$ denotes a vector of 1’s compatible with the dimensions of \mathbf{A} .

The first two constraints restrict the solution to a simplex and promote sparsity. The third constraint bounds the endmembers from above and implies that a material cannot reflect more than the incident radiation. Even if the image values do not represent reflectance, we can rescale the values in the range $[0 \dots 1]$.

The low geometric resolution HSRI can be modelled as a geometrically downsampled version of \mathbf{Z} :

$$\mathbf{H} \approx \mathbf{ZS} = \mathbf{EAS} = \mathbf{E}\tilde{\mathbf{A}}, \quad (4)$$

where $\mathbf{S} \in \mathbb{R}^{N_m \times N_h}$ is the downsampling operator that describes the spatial response of the hyperspectral sensor, and $\tilde{\mathbf{A}} \equiv \mathbf{AS}$ are the abundances at the lower resolution. \mathbf{S} can be approximated by taking the (possibly weighted) average values of the multispectral image corresponding to one HSRI pixel.

Likewise, the low spectral resolution HGRI can be modelled as a spectral downsampling of \mathbf{Z}

$$\mathbf{M} \approx \mathbf{RZ} = \mathbf{REA} = \tilde{\mathbf{E}}\mathbf{A}, \quad (5)$$

where $\mathbf{R} \in \mathbb{R}^{b \times B}$ is the spectral response function of the multispectral sensor and each row contains the responses of each multispectral band. $\tilde{\mathbf{E}} \equiv \mathbf{RE}$ are the spectrally transformed (downsampled) endmembers.

The fusion is solved if \mathbf{Z} has been found, which is the same as estimating \mathbf{E} and \mathbf{A} . Actually, by solving for \mathbf{E} and \mathbf{A} separately we are solving first the spectral unmixing and then using the result to generate the fused image \mathbf{Z} . By taking into account the constraints (3), we formulate the following constrained least-squares problem:

$$\arg \min_{\mathbf{E}, \mathbf{A}} \|\mathbf{H} - \mathbf{EAS}\|_F^2 + \|\mathbf{M} - \mathbf{REA}\|_F^2 \quad (6a)$$

$$\text{subject to } 0 \leq e_{ij} \leq 1, \quad \forall i, j \quad (6b)$$

$$a_{ij} \geq 0, \quad \forall i, j \quad (6c)$$

$$\mathbf{1}^\top \mathbf{A} = \mathbf{1}^\top \quad (6d)$$

with $\|\cdot\|_F$ denoting the Frobenius norm. To solve (6a) we propose to split it into two parts by computing for \mathbf{E} and \mathbf{A} from the HSRI and HGRI respectively. This is done in an iterative manner, by using a projected gradient approach and is described in detail in Lanaras et al. (2015).

3.2 Relative spectral response

The goal of this work is to estimate the relative spectral response of the multispectral sensor relative to the hyperspectral sensor given the HSRI and HGRI. The geometric and spectral downsamplings can be modelled as the matrices \mathbf{S} and \mathbf{R} . Theoretically, if one would spectrally degrade the HSRI and geometrically degrade the HGRI should end up with the exact same image. However, due to a number of effects and random errors this is not the case. We thus search for the two degradations (namely \mathbf{R} and \mathbf{S}), such that the differences of the created images are minimal. This corresponds to solving the following optimization problem, formulated as a least squares solution:

$$\arg \min_{\mathbf{R}, \mathbf{S}} \|\mathbf{RH} - \mathbf{MS}\|_F^2 \quad (7)$$

However, at this point we assume that \mathbf{S} is approximately known and does not affect the solution of \mathbf{R} . This is due to the fact that the images that we use are co-registered with each other and that the point spread function (PSF) effects of both sensors can be limited by applying a kernel to both images (Gaussian or averaging). That's why we will only optimize for \mathbf{R} . Additionally, the spectral responses of each multispectral channel are independent of each other. That means that e.g. estimating the response of the red channel is not affecting the response of the blue channel. Taking this fact into account, the estimation can be done separately for each multispectral band i as a linear combination of hyperspectral bands. We thus search for \mathbf{r}_i^\top , the i th row of \mathbf{R} , that contains the coefficients of the linear combination of the hyperspectral bands that contribute to the i th multispectral band.

$$\arg \min_{\mathbf{r}_i} \|\mathbf{r}_i^\top \mathbf{H} - \mathbf{M}_{i:} \mathbf{S}\|^2, \quad (8)$$

where $\mathbf{r}_i \in \mathbb{R}^B$, $\|\cdot\|$ is the l_2 vector norm and $\mathbf{M}_{i:}$ is the i th row of \mathbf{M} , that contains the i -band image. The solution to this least squares problem is the following.

$$\mathbf{r}_i = \mathbf{M}_{i:} \mathbf{S} \mathbf{H}^\top (\mathbf{H} \mathbf{H}^\top)^{-1} \quad (9)$$

3.2.1 Non-negativity of the spectral response. The simple least squares solution of (9) will actually most of the times give among others negative solutions for the values of the spectral response. This is not a realistic solution, because to synthesize an image you can only combine different wavelengths, but cannot use them in the sense that their contribution can be “negative”. To deal with this, we introduce a non-negative least squares problem instead.

$$\begin{aligned} \arg \min_{\mathbf{r}_i} \quad & \|\mathbf{r}_i^\top \mathbf{H} - \mathbf{M}_i \mathbf{S}\|^2 \\ \text{subject to} \quad & \mathbf{r}_i \geq 0, \end{aligned} \quad (10)$$

where inequality holds for every element of \mathbf{r}_i . This problem is solved with the MATLAB `lsqnonneg` routine, which uses the Lawson-Hanson algorithm.

3.2.2 Neighbouring bands. Additionally, in some cases where the noise is very dominant or other effects (e.g. multitemporal differences, atmospheric effects) influence the solution it is useful to assume that neighbouring wavelengths have a similar spectral response. For this case, we penalize results in neighbouring bands that differ a lot with each other. This is done by introducing a matrix $\mathbf{D} \in \mathbb{R}^{B-1 \times B}$ that computes a penalty term for the differences in neighbouring hyperspectral bands of the vector \mathbf{r}_i .

$$\begin{aligned} \arg \min_{\mathbf{r}_i} \quad & \|\mathbf{r}_i^\top \mathbf{H} - \mathbf{M}_i \mathbf{S}\|^2 + \lambda \|\mathbf{D} \mathbf{r}_i\|^2 \\ \text{subject to} \quad & \mathbf{r}_i \geq 0, \end{aligned} \quad (11)$$

To solve this optimization problem we implement an algorithm based on a primal-dual optimization with the alternating direction method of multipliers (ADMM). This is done to tackle the non-negativity of \mathbf{r}_i , by introducing a dual variable. The resulting \mathbf{r}_i depends on the value λ which controls the strength of the penalty and consequently the amount of smoothing. After optimizing for the parameter λ , we chose to use $\lambda = 10$ for all our experiments in 4.3.

4. RESULTS AND DISCUSSION

4.1 Datasets

To evaluate the proposed methodology we used data of APEX (Schaeppman et al., 2015), a hyperspectral sensor developed by a Swiss-Belgian consortium on behalf of ESA. APEX covers the spectral range 0.4-2.5 μm . We choose an image acquired in 2011 over Baden, Switzerland (true color composite in Figure 1), which has an GSD of approximately 2 m. The image was further cropped to have dimensions 400×400 pixels and only 211 spectral bands were kept, after removing water absorption bands. This image serves as reference data for the image fusion experiments.

4.1.1 Synthetic data without noise. To simulate the HSRI \mathbf{H} we downsample it with a factor of 8, which is a realistic difference between observed HSRI and HGRI. The downsampling is done by simple averaging over 8×8 pixel blocks. The HGRI \mathbf{M} can be simulated using the spectral response \mathbf{R} of an existing multispectral sensor. For this case, we choose to use the spectral response \mathbf{R} of the Leica ADS80 (it has RGB and NIR channels covering the range 420-920 nm). This is done because the latter has a few times better resolution than APEX and thus is suitable for the fusion. It can be also regarded as a challenging case since their spectra do not fully overlap. That means that as input we have only one real hyperspectral image (which we call the “reference data”), from which we generate a HSRI and a HGRI by geometric, respectively spectral downsampling.

4.1.2 Synthetic data with noise. For this second case, we proceed exactly as in 4.1.1, but we introduce two sources of errors. Firstly, we add white Gaussian noise in both HSRI and HGRI with a $\text{SNR} = 30$ dB. Secondly, we introduce a coregistration error (translation) of 0.3 pixels in each of the x- and y- directions. Finally, we investigate a case where both noise and coregistration errors are combined.

4.2 Image fusion

For the hyperspectral - multispectral fusion and spectral unmixing we used only the images without noise and compared our results against three methods (Wycoff et al., 2013, Akhtar et al., 2014, Simoes et al., 2015). In Figure 1, there is a visual comparison where we report excellent performance against the other state-of-the-art methods. Extended results and comparisons are included in Lanaras et al. (2015).

From the results of the fusion we were able to reconstruct a hyperspectral image that has 8×8 better geometric resolution than the input HSRI. Additionally, due to the integrated coupled spectral unmixing the method returns

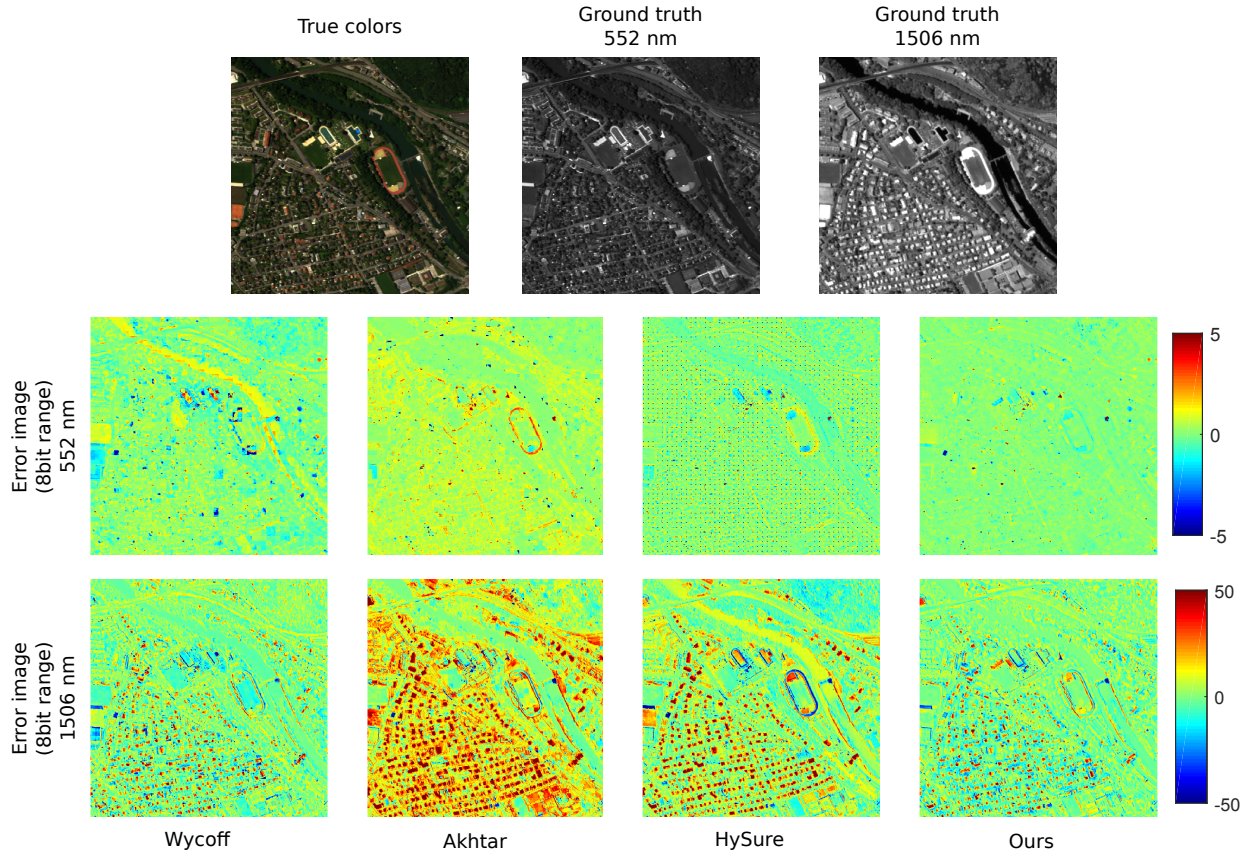


Figure 1. *Top row:* True color image of the APEX scene and ground truth spectral images for wavelengths 552 and 1506 nm. *Second and third rows:* The reflectance difference (in 8-bit range) between true and reconstructed image for each method at the two wavelengths. There is a difference in the color scale between the two rows.

a physically plausible set of the scene’s endmembers and their corresponding fractional abundances. In Figure 2 we show a specific case where we investigate (a) the stadium tartan and (b) a tennis court. On the top left is the abundance map for the endmember that corresponds to the tennis court from our method, while on the top right are the same abundance map, if we would only perform spectral unmixing given the HSRI. Clearly, the information that comes from the HGRI enables us to define the borders of different objects and improve the spectral unmixing, by defining the spatial distribution within each pixel. However, there is no way to quantitatively evaluate the unmixing quality, because no ground truth exists. In the bottom left are the abundances corresponding to the stadium tartan. Note that there are different values for these two different materials, although in the true color image (Figure 1) they have very similar color. On the bottom right are the spectra of the two test surfaces, averaged over 30 pixels, which were manually selected from the ground truth image. Although the two areas reflect very similarly in the visible spectrum, there is a big change in the infrared range.

4.3 Estimated spectral responses

As expected, the solution using unconstrained least squares (Figure 3), even without any introduced noise, does not deliver the expected results. All four channels seem to have a similar response, take extremely large values and have many negative values.

4.3.1 Data without noise. The results of this section are using the data specified in 4.1.1 and are an ideal case, which doesn’t hold in practice. We run the two algorithms (non-negative solution and the neighbouring bands constraint) in this case to study the “no noise” case. Actually in Figure 4 we can observe that in the absence of noise the result of the non-negative least squares (left) is identical with the true spectral response, which we used to create the synthetic data. On the other hand, the smoothing applied (right) creates a Gaussian-bell like curve, which however seems to fit well with the true values.

4.3.2 Data with noise. In the real-life scenario, the data to estimate the spectral response will contain many random or systematic errors. In Figure 5, we use the two algorithms to treat the three noise cases (see sec. 4.1.2). When noise is added to the images (a), we observe also noisy estimated spectral responses and also slightly widened (shifted to left and/or right) compared to the true values. With the smoothed version this “extended” values still

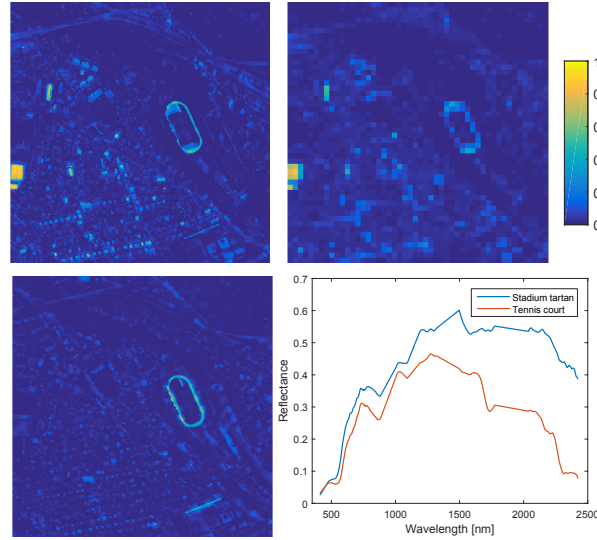


Figure 2. *Top row*: Abundance maps corresponding to the tennis court surface endmember: for the fused image (left), for the HSRI (right). *Bottom row*: Abundance map for the fused image corresponding to the endmember of the stadium tartan (left), the ground truth spectra (manually determined) of the respective materials (right).

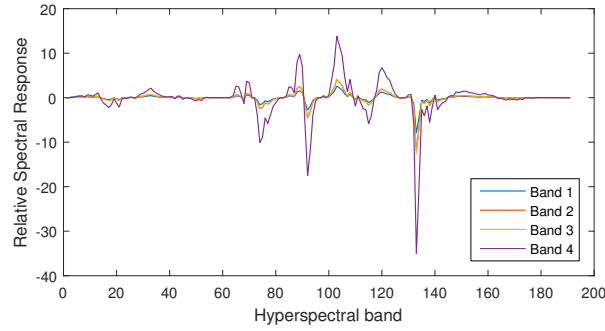


Figure 3. The solution using unconstrained least squares.

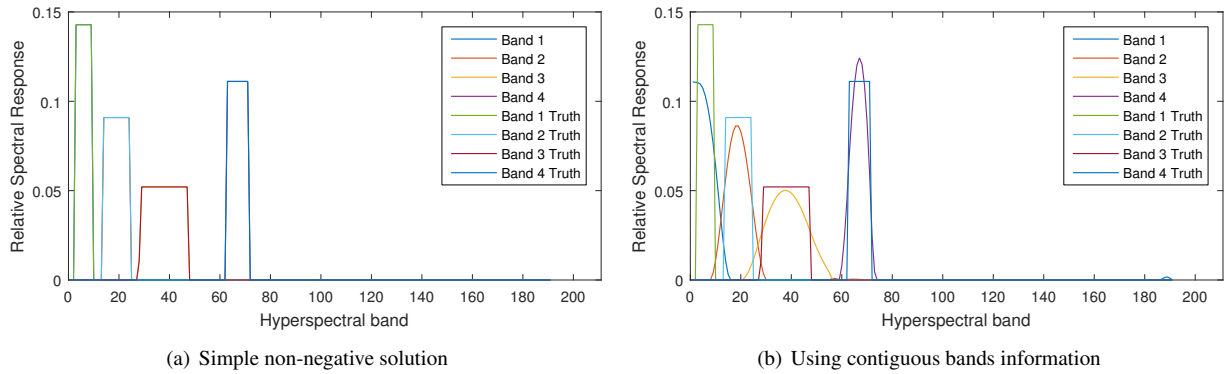
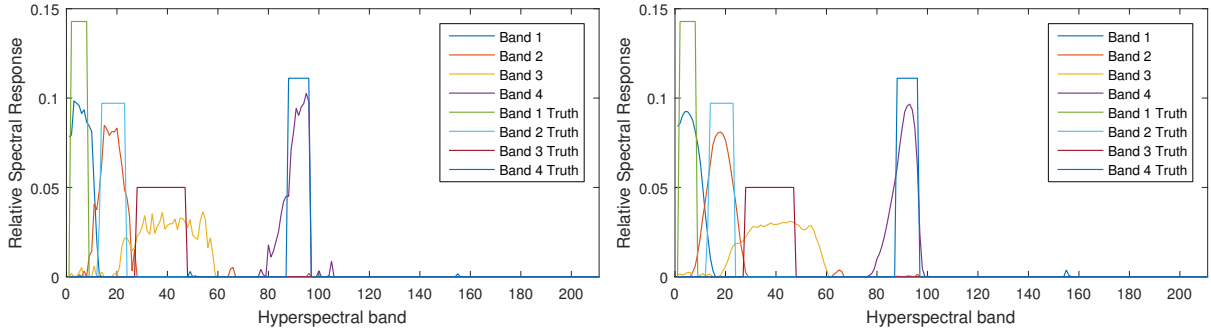
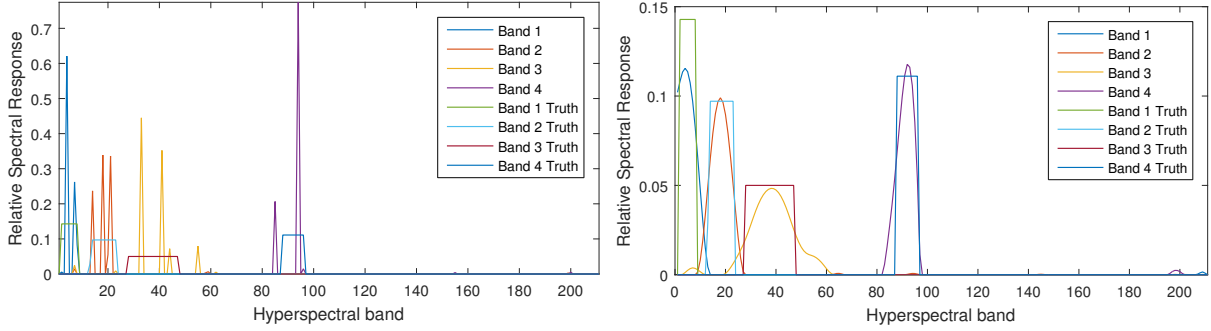


Figure 4. The estimated relative spectral response from images without noise.

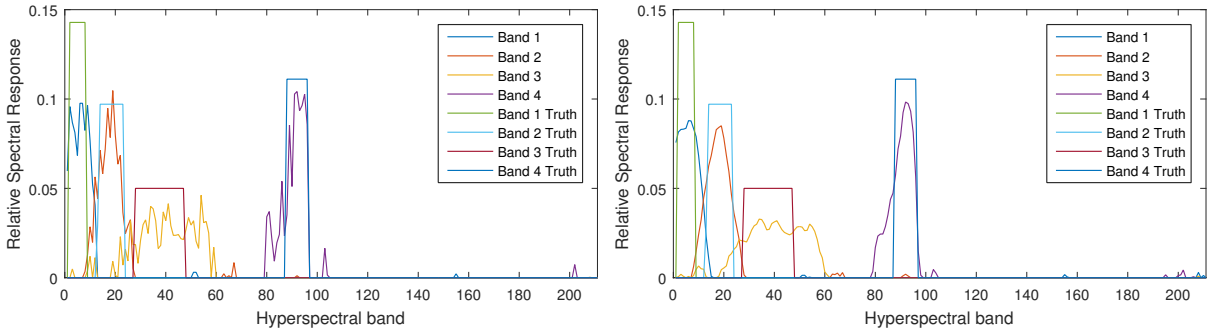
exist, but have limited noise. In the 0.3 pixels misregistration between the images (b) we observe some very high peaks (notice the difference between left and right plot in the axis scale), around the correct hyperspectral bands. In most cases the most dominant values correspond to only three hyperspectral bands. This implies that in this case the respective multispectral band is optimally recreated by those hyperspectral bands only. The smooth version on the right hand side now removes this effect and gives similar results to the case where there was no noise. In the last case (c) where both (a) and (b) are included, there seems to be a mix of effects. However, the smoothed version gives more convincing results. In the presented case, the true spectral responses have a rectangular shape. This rectangular form is rather modelled in our solution by a Gaussian curve, due to the neighbouring band constraint. We believe that in the case the shape of the spectral response varies gradually this constraint will provide results closer to the true spectral response.



(a) Images with noise 30 dB



(b) Coregistration 0.3 pixels misaligned



(c) Both previous effects (a), (b)

Figure 5. *Left column*: Solution with non-negative least squares, *Right column*: Solution with the smoothed version

5. CONCLUSIONS AND FUTURE WORK

Firstly, in this work we perform an integrated processing of both HSRI and HGRI to jointly solve the tasks of image fusion and spectral unmixing. Thereby, the spectral unmixing supports image fusion and vice versa. During this joint estimation, we enforce several useful physical constraints simultaneously, which lead to a more plausible estimation of endmembers and abundances, and at the same time improve the fusion. Secondly, we estimate the relative spectral response of the two sensors, a procedure which can make the fusion process independent from having any prior information about the two sensor responses.

In future work, we plan to use real data to estimate the spectral response and compare the solution with the known spectral responses of the two sensors. Another step is to incorporate in the model pixels that can be considered as outliers, due to various effects (e.g. multitemporal differences, specular reflections) and reweight or exclude them from the solution. We also aim to estimate the point spread function of the multispectral image, by computing the matrix \mathbf{S} along with the spectral response and finally to integrate this process with the fusion in one optimization, from which all unknown parameters will be estimated.

ACKNOWLEDGEMENTS

We would like to thank the Remote Sensing Laboratories of University of Zurich for providing the data and useful discussions.

REFERENCES

- Akhtar, N., Shafait, F. and Mian, A., 2014. Sparse spatio-spectral representation for hyperspectral image super-resolution. In: *Computer Vision–ECCV 2014*, Springer, Heidelberg, pp. 63–78.
- Bioucas-Dias, J. M., Plaza, A., Dobigeon, N., Parente, M., Du, Q., Gader, P. and Chanussot, J., 2012. Hyperspectral unmixing overview: Geometrical, statistical, and sparse regression-based approaches. *IEEE Journal of Selected Topics in Applied Earth Observations and Remote Sensing* 5(2), pp. 354–379.
- Hardie, R. C., Eismann, M. T. and Wilson, G. L., 2004. Map estimation for hyperspectral image resolution enhancement using an auxiliary sensor. *IEEE Trans. on Image Processing* 13(9), pp. 1174–1184.
- Keshava, N. and Mustard, J. F., 2002. Spectral unmixing. *IEEE Signal Processing Magazine* 19(1), pp. 44–57.
- Lanaras, C., Baltsavias, E. and Schindler, K., 2015. Advances in hyperspectral and multispectral image fusion and spectral unmixing. In: *ISPRS - International Archives of the Photogrammetry, Remote Sensing and Spatial Information Sciences*, Vol. XL-3/W3, pp. 451–458.
- Schaepman, M. E., Jehle, M., Hueni, A., D’Odorico, P., Damm, A., Weyermann, J., Schneider, F. D., Laurent, V., Popp, C., Seidel, F. C., Lenhard, K., Gege, P., Kuechler, C., Brazile, J., Kohler, P., Vos, L. D., Meuleman, K., Meynart, R., Schlaepfer, D., Kneubuehler, M. and Itten, K. I., 2015. Advanced radiometry measurements and earth science applications with the airborne prism experiment (APEX). *Remote Sensing of Environment* 158, pp. 207–219.
- Simoes, M., Bioucas-Dias, J., Almeida, L. and Chanussot, J., 2015. A convex formulation for hyperspectral image superresolution via subspace-based regularization. *IEEE Trans. on Geoscience and Remote Sensing* 53(6), pp. 3373–3388.
- Wei, Q., Dobigeon, N. and Tournieret, J.-Y., 2014. Bayesian fusion of hyperspectral and multispectral images. In: *IEEE International Conference on Acoustics, Speech and Signal Processing (ICASSP)*, IEEE, pp. 3176–3180.
- Wycoff, E., Chan, T.-H., Jia, K., Ma, W.-K. and Ma, Y., 2013. A non-negative sparse promoting algorithm for high resolution hyperspectral imaging. In: *IEEE International Conference on Acoustics, Speech and Signal Processing (ICASSP)*, IEEE, pp. 1409–1413.
- Yokoya, N., Mayumi, N. and Iwasaki, A., 2013. Cross-calibration for data fusion of eo-1/hyperion and terra/aster. *IEEE Journal of Selected Topics in Applied Earth Observations and Remote Sensing* 6(2), pp. 419–426.
- Yokoya, N., Yairi, T. and Iwasaki, A., 2012. Coupled nonnegative matrix factorization unmixing for hyperspectral and multispectral data fusion. *IEEE Trans. on Geoscience and Remote Sensing* 50(2), pp. 528–537.